Med Biol Eng Comput (2017) 55:2183–2195
DOI 10.1007/s11517-017-1656-4

ORIGINAL ARTICLE

# Conformal mapping of carotid vessel wall and plaque thickness measured from 3D ultrasound images

**Gary P. T. Choi[1] · Yimin Chen[2] · Lok Ming Lui[3] · Bernard Chiu[2]**

Received: 5 April 2017 / Accepted: 13 May 2017 / Published online: 7 June 2017


**Abstract** Measurements of vessel-wall-plus-plaque thickness (*VWT*) from 3D carotid ultrasound have been shown to be sensitive to the effect of pharmaceutical interventions. Since the geometry of carotid arteries is highly subject-specific, quantitative comparison of the distributions of point-wise *VWT* measured for different patients or for the same patients at different ultrasound scanning sessions requires the development of a mapping strategy to adjust for the geometric variability of different carotid surface models. In this paper, we present an algorithm mapping each 3D carotid surface to a 2D carotid template with an emphasis on preserving the local geometry of the carotid surface by minimizing local angular distortion. The previously described arc-length scaling (AL) approach was applied to generate an initial 2D *VWT* map. Using results established in the quasi-conformal theory, a new map was computed to compensate for the angular distortion incurred in AL mapping. As the 2D carotid template lies on an L-shaped non-convex domain, one-to-one correspondence of the mapping operation was not guaranteed. To address this issue, an iterative Beltrami differential chopping and smoothing procedure was developed to enforce bijectivity. Evaluations performed in the 20 carotid surface models showed that the reduction in average angular distortion made by the proposed algorithm was highly significant ($P = 2.06 \times 10^{-5}$). This study is the first study showing that a bijective conformal map to a non-convex domain can be obtained using the iterative Beltrami differential chopping and smoothing procedure. The improved consistency exhibited in the 2D *VWT* map generated by the proposed algorithm will allow for unbiased quantitative comparisons of *VWT* as well as local geometric and hemodynamic quantities in population studies.

**Keywords** 3D ultrasound · Carotid atherosclerosis · 2D carotid template · 2D vessel-wall-plus-plaque thickness (*VWT*) map · Conformal mapping

## 1 Introduction

Stroke is one of the leading causes of death and disability worldwide, with 17.3 million people suffering a stroke each year [33]. Over two thirds of stroke mortality occurred in the developing countries [29]. As the most populous developing country, China has an annual stroke mortality of 1.6 million [28], and a stroke mortality rate that is seven times higher than that in the USA in the age group of 40–64 [22]. Carotid atherosclerosis is a major source of thrombosis and subsequent emboli, which may travel and block one of the cerebral arteries, causing ischemic stroke [16]. Fortunately, for patients with high risk of stroke, management of carotid atherosclerosis through lifestyle changes, dietary and medical treatments can prevent 75–80% of strokes [35]. Therefore, improved strategies for identification of patients at high risk of stroke and the development of sensitive and cost-effective techniques in evaluating treatment efficacy will have an enormous impact in patient management.

✉ Bernard Chiu
bcychiu@cityu.edu.hk

[1] John A. Paulson School of Engineering and Applied Sciences, Harvard University, Cambridge, MA, USA

[2] Department of Electronic Engineering, City University of Hong Kong, Hong Kong, Hong Kong

[3] Department of Mathematics, The Chinese University of Hong Kong, Hong Kong, Hong Kong

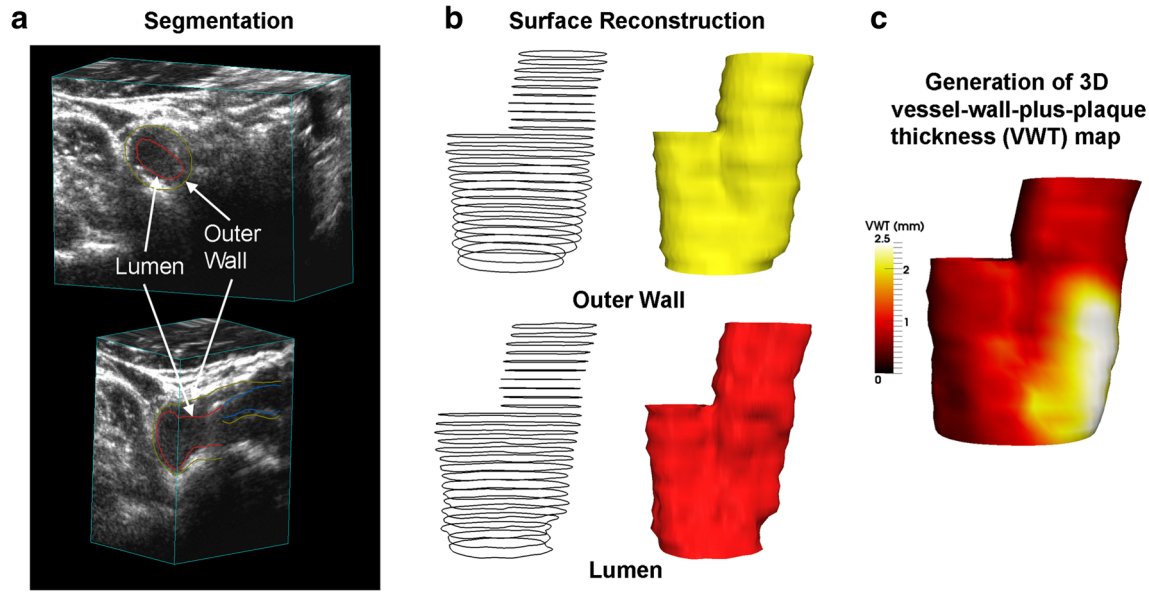


**Fig. 1** Steps involved in the generation of 3D vessel-wall-plus-plaque thickness (*VWT*) map

Measurements of carotid stenosis and intima media thickness (IMT) based on 2D B-mode ultrasound images have been widely used in the the assessment of carotid atherosclerosis. However, clinical trials based on these two measurements require a large sample size to achieve statistical significance of treatment options. Moreover, these two measurements are prone to variability as they are measured based on 2D cross sections selected by operators. The development of 3D carotid ultrasound has allowed physicians to examine the 3D anatomical structure of carotid artery and has been shown to produce reproducible measurements of total plaque volume (TPV) [1, 26] and vessel wall volumes (VWV) [15, 24]. However, these volumetric measurements did not take into account the spatial distribution of progression/regression of atherosclerosis. As carotid atherosclerosis is a focal disease predominantly occurring at the bifurcation and the carotid bulb regions [25, 27, 31], measurement tools that consider spatial distribution of plaque and vessel wall changes may lead to a more sensitive assessment of treatment effects and more accurate risk assessment. To quantify the spatial distribution of vessel wall and plaque thickness change (*VWT-Change*), we have previously described an approach to map point-wise *VWT-Change* onto the 3D carotid surface, which we referred to as the 3D *VWT-Change* map [9] (Fig. 1). However, because the geometry of 3D carotid surfaces is highly subject-specific, *VWT-Change* distributions of subjects undergone different therapies or of the same subject derived from different imaging modalities were compared by qualitative visual matching in previous clinical studies [15, 23, 24]. To adjust for the anatomic variability of the carotid arteries across patients, we developed an arc-length scaling approach, referred to as the AL approach hereafter, that mapped 3D *VWT-Change* maps (Fig. 2a) to an L-shaped carotid template [10] (Fig. 2b) by scaling the arc-length of transverse contours segmented from 2D transverse images resliced from 3D ultrasound images.

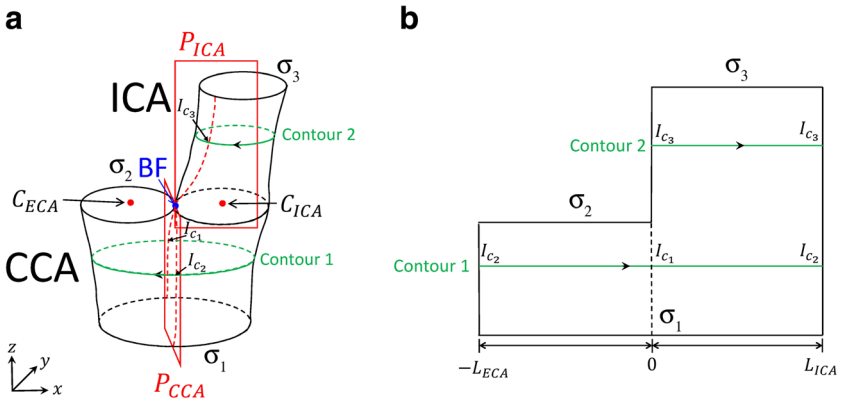


**Fig. 2** Schematic illustrating the 2D arc-length scaling (AL) approach. The carotid surface shown in (**a**) was cut by two planes, denoted by $P_{ICA}$ and $P_{CCA}$, and unfolded to a planar L-shaped non-convex domain as shown in (**b**)

However, the AL mapping approach was developed without considering geometric distortion introduced by the 3D to 2D mapping. It is widely recognized that surface mapping introduces angular and/or area distortions unless the Gaussian curvature is zero everywhere [20]. Previous conformal or angle-preserving mapping strategies have been proposed for both non-bifurcating [21] and bifurcating [39] tubular surfaces. These approaches solved a longitudinal and a circumferential Dirichlet problem to achieve conformity, but are not suitable for carotid template construction for several reasons. First, regional correspondence was not taken into account in the development of the conformal colon surface mapping algorithm described by Haker et al. [21] as the boundary conditions was set to 0 and 1 at the inlet and outlet of the colon surfaces, respectively, for the longitudinal Dirichlet problem, effectively scaling the length of all colons to unity in the resulting conformal maps without considering the physical lengths of individual colons. Zhu et al. [39] addressed this issue by generating a centerline of each bifurcating vessel and estimated the boundary conditions at the inlet and outlet based on the length of the centerline. However, both techniques generated conformal maps with shapes dependent on the geometry of the original 3D surfaces, rendering them not suitable for the purpose of carotid template construction. Antiga et al. [3] split the common, internal and external carotid arteries (CCA, ICA and ECA, respectively) and mapped each artery to a standard rectangular domain. For each artery, they first solved the longitudinal Dirichlet problem with boundary conditions assigned in the same way as Haker et al. [21]. To address the surface correspondence issue, they stretched the resulting longitudinal parameterization according to the length of the centreline. Instead of solving the circumferential Dirichlet problem, the circumferential parameterization was defined by the angle each surface point made with the centreline. Due to the stretching and the use of the angular circumferential parameterization, the resulting map was not a conformal map. Moreover, since the flattened maps for CCA, ICA and ECA were generated independently, local hemodynamic distribution in the vicinity of the bifurcating region was displayed in three highly discontinuous sections. This is a significant disadvantage of this mapping technique if used for *VWT* assessment as plaques appear predominantly at the bifurcation and the carotid bulb.

In this paper, we present a fast algorithm to map 3D *VWT* maps to a 2D carotid template that preserves the local geometry in the sense of preserving angles at an infinitesimal scale. Our goal for developing this new mapping approach is to improve the geometric consistency of the 2D carotid template so as to allow for more accurate comparison and quantification of *VWT* maps obtained at different times for each patient as well as for different patients in population studies. The specific approach involves correcting the angular distortion arising from the previous described AL mapping approach using established results from quasi-conformal theories. As the AL maps serve as the initial maps in the proposed framework, the new maps remain to be continuous from CCA to ICA and the longitudinal distance of a point from the bifurcation is approximately maintained. Since the proposed algorithm allows for the specification of landmark constraints, the shapes of the AL maps are retained after the correction of angular distortion, and therefore, the shapes of the new maps are still standardized across patients. Although mapping algorithms based on quasi-conformal theories have been proposed, mapping to the AL map sitting on a non-convex L-shaped domain represents a unique challenge. Previously described mapping algorithms were all designed to map to a convex domain. Zeng et al. [38] developed a quasi-conformal flattening algorithm for colon surfaces onto a rectangular domain and later extended the algorithm to map general Riemann surfaces onto the unit disk or a rectangular domain using discrete curvature flow [37]. Choi and Lui [12, 14] proposed conformal surface flattening algorithms to map simply-connected open surfaces onto the unit disk using composites of quasi-conformal maps. For the non-convex L-shaped domain involved in carotid template generation, there is no guarantee that these quasi-conformal mapping approaches would generate bijective maps. A major technical contribution of this paper is the development and validation of a mapping technique that guarantees bijectivity when mapping from the 3D carotid surface to the non-convex planar carotid template.

## 2 Materials and methods

### 2.1 Study subjects and image acquisition

Ten subjects with carotid atherosclerosis were involved in this study. These subjects were recruited from The Premature Atherosclerosis Clinic at University Hospital (London Health Science Center, London, Canada) and the Stroke Prevention & Atherosclerosis Research Center, Robarts Research Institute. These subjects were scanned at baseline and 2 weeks later with a 3D ultrasound carotid imaging system previously described [17], thereby providing 20 images for the evaluation of the proposed algorithm.

### 2.2 Construction of the 3D vessel-wall-plus-plaque thickness change (*VWT-Change*) map

The 3D *VWT-Change* map construction algorithm was described in detail previously [8–10] and briefly summarized in the schematic shown in Fig. 1. The 3D ultrasound carotid images were resliced at 1-mm interval perpendicular to the medial axis of the vessel identified by an expert

observer. The expert observer segmented the outer wall and the lumen of the carotid artery on each resliced image as shown in Fig. 1a. The lumen and vessel wall surfaces were reconstructed from the segmented boundary stacks as shown in Fig. 1b using a previously described technique [9]. To reduce the effect of segmentation variability, the lumen and outer wall boundaries were repeatedly segmented for five times, with consecutive segmentation sessions separated by at least 24 h to minimize observer memory bias. The mean lumen and outer wall surfaces for repeated segmentations were computed using a previously described technique [9, 11]. The mean outer wall and lumen surfaces were matched on a point-by-point basis using a previously described surface correspondence algorithm [9]. Vessel-wall-plus-plaque thickness (*VWT*) was measured by taking the distance between each pair of correspondence points on the wall and lumen surfaces. Figure 1c shows the outer wall surface with *VWT* colour-coded and superimposed.

### 2.3 Generation of the conformal 2D carotid template

Figure 3 shows the schematic of the proposed algorithm for carotid template generation. The carotid map generated by the arc-length scaling (AL) approach [10] served as the initial map. Then, a map was computed based on the quasi-conformal mapping theory to correct for the angular distortion incurred in AL mapping. Finally, an iterative scheme was applied to enforce bijectivity of the mapping operation.

#### *2.3.1 2D arc-length scaling (AL) map*

The 2D arc-length scaling (AL) map has been described in detail elsewhere [8, 10, 11] and is briefly described here. The first step of this algorithm involves transforming the 3D carotid surface to a standard coordinate system with the bifurcation (BF) located at the origin and the longitudinal direction of common carotid artery (CCA) aligned with the $z$-axis. Centroids denoted by $C_{ECA}$ and $C_{ICA}$ in Fig. 2a were obtained from the external and internal carotid contours that were closest to the bifurcation, and the line from $C_{ECA}$ and $C_{ICA}$ was aligned with the $x$-axis.

Then, the ICA and CCA of the 3D carotid surface were cut by two planes, labelled as $P_{ICA}$ and $P_{CCA}$ in Fig. 2a, respectively, and unfolded into a 2D L-shaped domain as shown in Fig. 2b. The CCA inlet and the ECA and ICA outlets, denoted by $\sigma_1$, $\sigma_2$ and $\sigma_3$, were mapped to the bottom and top edges of the 2D AL map as shown in Fig. 2.

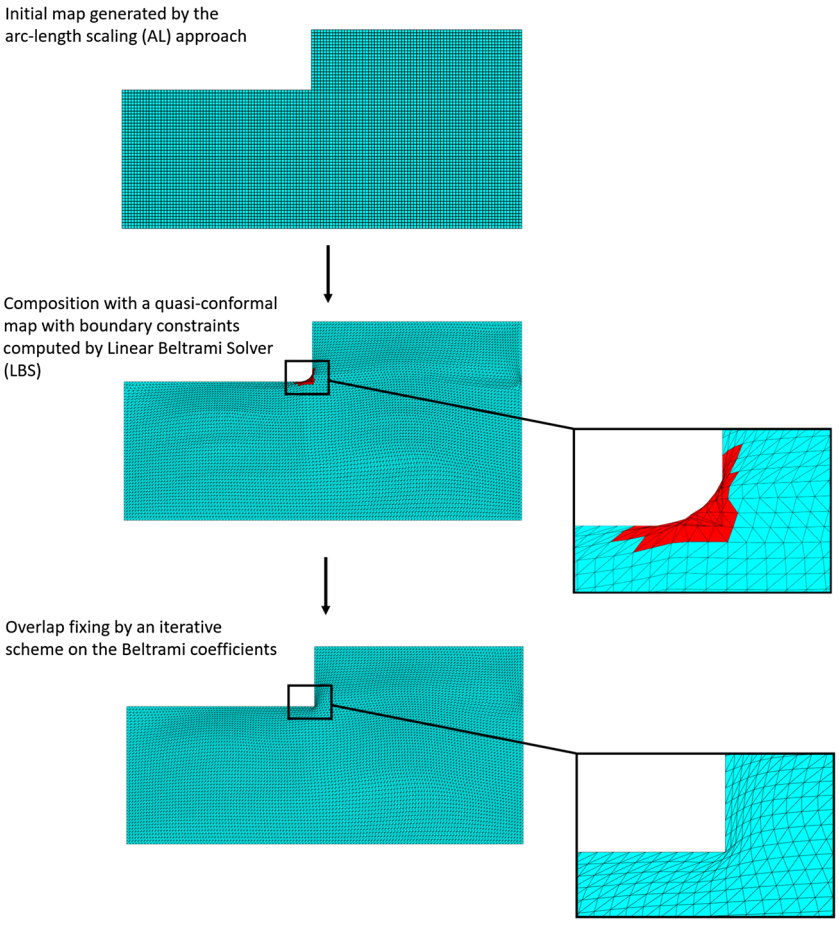


**Fig. 3** Flowchart of the proposed conformal mapping approach

Figure 2a also shows two example contours on the CCA and ICA surfaces, labelled as Contours 1 and 2, respectively, which were mapped to two straight lines shown in Fig. 2b.

The width of the 2D map was determined by first dividing each 3D carotid surface into the two surfaces: one including half of the CCA and the entire ICA (red surface in Fig. 4a), referred to as the ICA surface hereafter for easy reference, and the other including the other half of CCA (blue surface in Fig. 4a), referred to as the wo-ICA surface, standing for without ICA. The average surface areas of the ICA and wo-ICA surfaces were computed over the entire cohort of patients involved in the study. The width of the ICA side of the 2D AL template, denoted by $L_{ICA}$, was designed such that its area (red region in Fig. 4b) is equal to the average ICA surface area for the entire cohort under investigation. The width on the wo-ICA side of the 2D AL template, denoted by $L_{wo-ICA}$, was calculated in a similar manner.

### 2.3.2 Conformal mapping

Since the proposed conformal mapping algorithm was developed based on quasi-conformal theory, we provide a brief description of this theory and on the construction of a quasi-conformal map before laying out the proposed conformal algorithm developed for carotid template generation.

Quasi-conformal mapping is a generalization of conformal mapping. Specifically, a map $f : \mathbb{C} \to \mathbb{C}$ is a quasi-conformal map if it satisfies the Beltrami equation:

$$\frac{\partial f}{\partial \overline{z}} = \mu(z)\frac{\partial f}{\partial z} \tag{1}$$

for some complex-valued function $\mu$ which satisfies $\lim_{p\to\infty}\left(\int |\mu|^p\right)^{1/p} < 1$ and that $\frac{\partial f}{\partial z}$ is non-vanishing almost everywhere. Here, the complex partial derivatives are defined by

$$\frac{\partial f}{\partial z} := \frac{1}{2}\left(\frac{\partial f}{\partial x} - i\frac{\partial f}{\partial y}\right) \quad \text{and} \quad \frac{\partial f}{\partial \overline{z}} := \frac{1}{2}\left(\frac{\partial f}{\partial x} + i\frac{\partial f}{\partial y}\right). \tag{2}$$

$\mu$ is called the *Beltrami coefficient* of the quasi-conformal map $f$. The Beltrami coefficient serves as a measure of the conformality of a map. In particular, the quasi-conformal map $f$ is conformal around a small neighborhood of a point $p$ if and only if $\mu(p) = 0$.

One important property of quasi-conformal maps is related to the Beltrami coefficient of composition maps. Suppose $f : \Omega_1 \to \Omega_2$ and $g : \Omega_2 \to \Omega_3$ are two quasi-conformal maps with the Beltrami coefficients $\mu_f$ and $\mu_g$, respectively. The Beltrami coefficient of the composition map $g \circ f : \Omega_1 \to \Omega_3$ is given by

$$\mu_{g\circ f} = \frac{\mu_f + \frac{\overline{f_z}}{f_z}(\mu_g \circ f)}{1 + \frac{\overline{f_z}}{f_z}\overline{\mu_f}(\mu_g \circ f)}, \tag{3}$$

where $f_z = \frac{\partial f}{\partial z}$ and $\overline{f_z}$ is the complex conjugate of $f_z$.

The above concept of quasi-conformal maps between planar complex domains can be naturally extended to Riemann surfaces. For every point $x$ on a Riemann surface, there exists a neighborhood of $x$ (denoted by $U_x$) and a homeomorphism $\phi_x : U_x \to \mathbb{C}$ which maps $U_x$ to a region on the complex plane. In other words, a Riemann surface looks like a patch of the complex plane locally near every point. $(U_x, \phi_x)$ is called a local chart. A map $f : M \to N$ between two Riemann surfaces $M$ and $N$ is said to be quasi-conformal if for any local chart $(U_\alpha, \phi_\alpha)$ on $M$ and any local chart $(U_\beta, \psi_\beta)$ on $N$, the map $\psi_\beta \circ f \circ \phi_\alpha^{-1} : \phi_\alpha(U_\alpha \cap U_\beta) \subset \mathbb{C} \to \psi_\beta(U_\alpha \cap U_\beta) \subset \mathbb{C}$ is quasi-conformal. We collect the Beltrami coefficients of all these

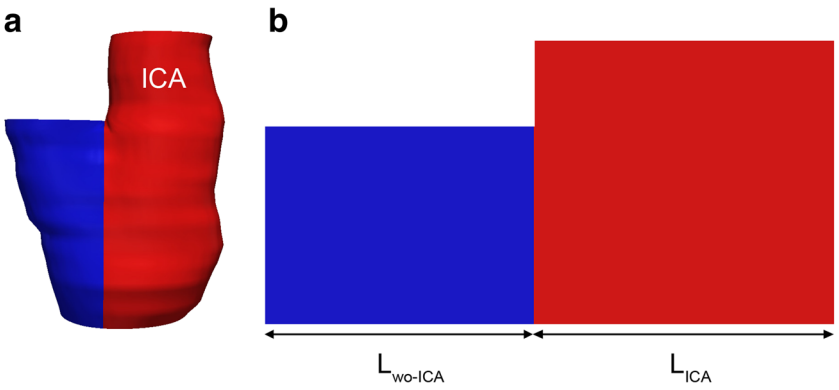


**Fig. 4** Schematic illustrating how the width of the 2D carotid template was determined. **a** Each carotid surface was divided into two parts: The *red surface* with half of the CCA and the entire ICA and the *blue surface* with remaining half of the CCA. Average areas of the *red* and *blue surfaces* over the entire cohort were computed. **b** $L_{ICA}$ and $L_{wo-ICA}$ were computed to make the *red* and the *blue areas* in the 2D carotid template equal to the corresponding average areas over the entire cohort of 3D carotid models

planar maps, and the collection is called the Beltrami differential of the quasi-conformal map $f$. Equation 3 is central to the quasi-conformal mapping approach applied in this paper as it gives rise to the following theorem [13]:

*Let $f : M_1 \to M_2$ and $g : M_2 \to M_3$ be quasi-conformal maps. Suppose the Beltrami differential of $f^{-1}$ and $g$ are the same. Then the Beltrami differential of $h = g \circ f$ is equal to 0. Hence, $h = g \circ f : M_1 \to M_3$ is conformal.*

For generation of the conformal carotid template, we suppose $f : S \to L$ represents the 2D AL map described in Section 2.3.1, where $S$ denotes the carotid surface and $L$ denotes the L-shaped planar domain. The Beltrami differential of $f^{-1}$ can be computed using the formula $\mu_{f^{-1}}(u,v) = \frac{E-G+2iF}{E+G+2\sqrt{EG-F^2}}$, where $\begin{pmatrix} E & F \\ F & G \end{pmatrix}$ represents the first fundamental form. Particularly, with $f^{-1}(u,v)$ expressed by$(X(u,v), Y(u,v), Z(u,v))$, $E = \left(\frac{\partial X}{\partial u}\right)^2 + \left(\frac{\partial Y}{\partial u}\right)^2 + \left(\frac{\partial Z}{\partial u}\right)^2$, $F = \frac{\partial X}{\partial u}\frac{\partial X}{\partial v} + \frac{\partial Y}{\partial u}\frac{\partial Y}{\partial v} + \frac{\partial Z}{\partial u}\frac{\partial Z}{\partial v}$, and $G = \left(\frac{\partial X}{\partial v}\right)^2 + \left(\frac{\partial Y}{\partial v}\right)^2 + \left(\frac{\partial Z}{\partial v}\right)^2$. According to the above theorem, the construction of a conformal map $h$ comes down to finding a map $g$ that has the same Beltrami differential as $f^{-1}$. Based on this prescribed Beltrami differential, the mapping $g : L \to L$ can be reconstructed by the Linear Beltrami Solver (LBS) [30]. Mapping to boundary points of the 2D carotid template by the AL approach was retained by imposing landmark constraints. The landmark-constrained LBS algorithm is briefly described below:

Let $\mu_{f^{-1}} = \rho + i\tau$. We aim to compute a map $g : L \to L$ with $\mu_g = \rho + i\tau$. Let $g = u + iv$. By substituting these expressions into the Beltrami equation (Eq. 1), the partial derivatives $v_x, v_y, u_x, u_y$ are related by the following equations:

$$\begin{array}{ll} v_y = \alpha_1 u_x + \alpha_2 u_y; & -u_y = \alpha_1 v_x + \alpha_2 v_y; \\ -v_x = \alpha_2 u_x + \alpha_3 u_y, & u_x = \alpha_2 v_x + \alpha_3 v_y, \end{array} \quad \text{and} \quad (4)$$

where $\alpha_1 = \frac{(\rho-1)^2+\tau^2}{1-\rho^2-\tau^2}$; $\alpha_2 = -\frac{2\tau}{1-\rho^2-\tau^2}$; $\alpha_3 = \frac{(1+\rho)^2+\tau^2}{1-\rho^2-\tau^2}$. Since $\nabla \cdot \begin{pmatrix} v_y \\ -v_x \end{pmatrix} = v_{xy} - v_{xy} = 0$ and $\nabla \cdot \begin{pmatrix} -u_y \\ u_x \end{pmatrix} = -u_{xy} + u_{xy} = 0$, $g$ can be computed by solving the following equations

$$\nabla \cdot \left( A \begin{pmatrix} u_x \\ u_y \end{pmatrix} \right) = 0 \quad \text{and} \quad \nabla \cdot \left( A \begin{pmatrix} v_x \\ v_y \end{pmatrix} \right) = 0, \quad (5)$$

where $A = \begin{pmatrix} \alpha_1 & \alpha_2 \\ \alpha_2 & \alpha_3 \end{pmatrix}$. In the discrete case, the above equations can be discretized into sparse symmetric positive definite linear systems, which can be efficiently solved. The prescribed landmark constraints can be imposed in the linear systems.

Since the L-shaped planar domain $L$ is non-convex, the conformal map $h$ computed is not guaranteed to be bijective. In particular, there may be fold-overs near the sharp corner of the L-shaped domain (Fig. 3). An important result in quasi-conformal theory states that a map is bijective only if its Beltrami differential is smaller than unity everywhere, as explained in [14] using the Jacobian of the map. To enforce bijectivity, we applied an algorithm to smooth and chop the Beltrami differential iteratively until bijectivity of the map was achieved [13]. Specifically, we obtained the Beltrami differential of $h^{-1}$, denoted by $\nu$, and then smoothed $\nu$ by minimizing the following energy function:

$$\tilde{\mu} = \arg\min_{\mu} \int (|\nabla \mu|^2 + |\mu - \nu| + |\mu|^2). \quad (6)$$

Then, $|\tilde{\mu}|$ was chopped down as follows if $\sup\{|\tilde{\mu}|\} \geq 1$:

$$|\tilde{\mu}| \leftarrow \min\{|\tilde{\mu}|, 1 - \epsilon\}, \quad (7)$$

where $\epsilon$ is a small positive number set to be 0.03 in this paper. With the prescribed Beltrami differential $\tilde{\mu}$ obtained, we reconstructed a map $\gamma : L \to L$ using the LBS algorithm described above. Since the smoothness of $\tilde{\mu}$ is lost after the chopping operation, we smoothed Beltrami differential of the map $\gamma$ by Eq. 6 again. The iteration continued until the resulting conformal map $F = \gamma \circ h$ becomes bijective with no fold-overs.

The following list summarizes the proposed bijective conformal mapping approach:

- Step 1: Construct the initial 2D map, $f$, using the AL approach.
- Step 2: Compute the Beltrami differential of $f^{-1}$ and denote it by $\mu$.
- Step 3: Compute a quasi-conformal map $g$ with the prescribed Beltrami coefficient $\mu$ using the LBS algorithm. Then, apply $g$ to the 2D AL map constructed in Step 1. By the composition formula (3), $h = g \circ f : S \to L$ is angle-preserving.
- Step 4: Compute the Beltrami differential of $h^{-1}$ (denoted by $\nu$), and solve the energy minimization problem in Eq. 6 to obtain $\tilde{\mu}$. Chop down the norm of $\tilde{\mu}$ and reconstruct a map $\gamma$ using the LBS algorithm. Compute the Beltrami coefficient of $\gamma$ and repeat Step 4 until the resulting conformal map $F = \gamma \circ h$ is bijective and with no fold-overs.

## 3 Results

The first column of Fig. 5 shows six example carotid models from four subjects with *VWT* colour-coded and superimposed. Each figure shows an arterial model's near-side and a far-side view from the transducer. We will refer to the arteries displayed in Fig. 5 as Arteries A to D according to the first letter of the sub-figure labels. Two carotid models were acquired for Artery A at baseline and follow-up,

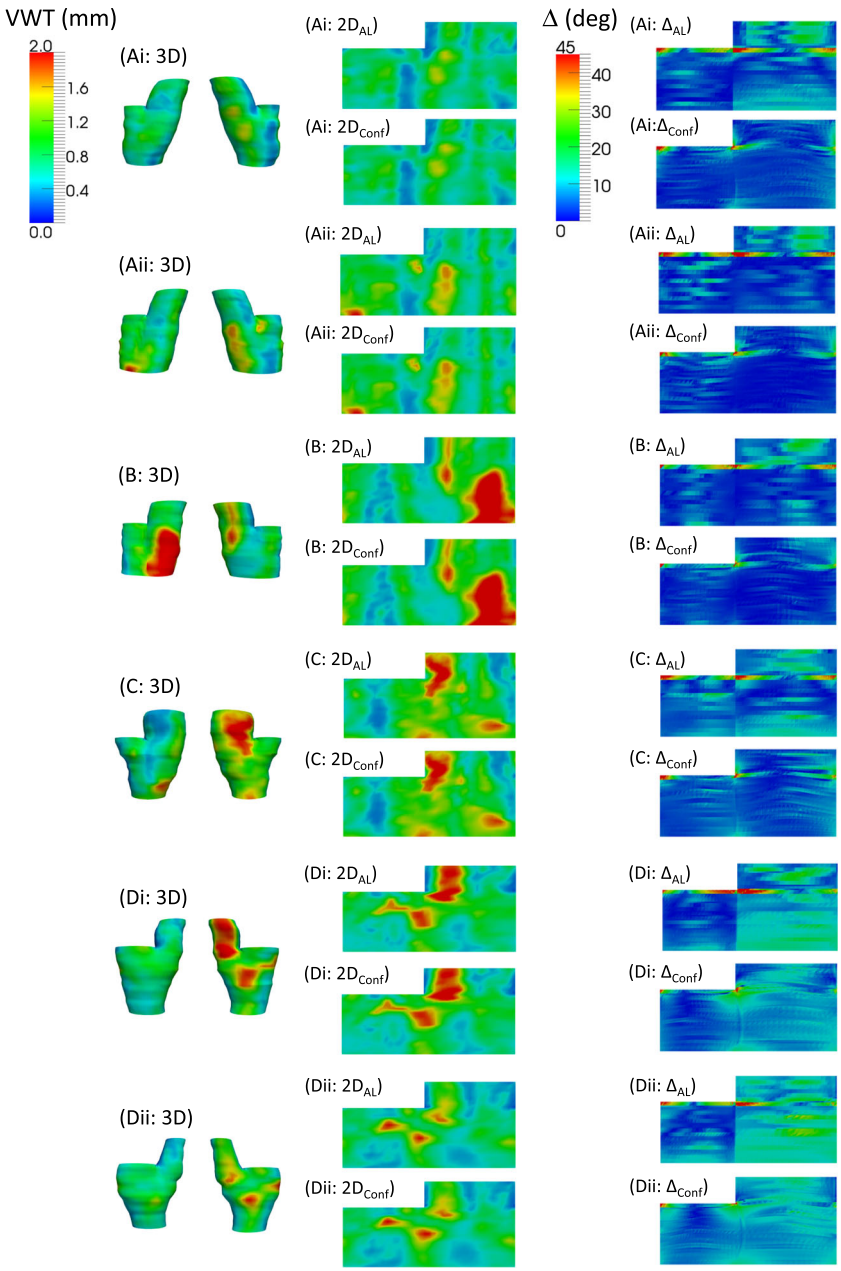


**Fig. 5** The 3D *VWT* maps (*first column*), the 2D *VWT* maps (*second column*) and the angular distortion map (*third column*) of six example carotid models from four subjects labelled A to D. The angular distortion for each triangular element in the map is denoted by $\Delta$ throughout the paper. The colour codes used for displaying VWT and angular distortion measurements are defined by the *colour bars* in the first row and used for all sub-figures. Carotid models Ai and Aii shown in the first two rows are models acquired at baseline and follow-up for Artery A, and carotid models Di and Dii shown in the last two rows are models acquired at baseline and follow-up for Artery D. The top sub-figures in the second and third columns show the 2D *VWT* and angular distortion maps for the previously described AL mapping algorithm [10, 11], and the bottom sub-figures show the maps associated with the proposed conformal mapping algorithm

labelled as Models Ai and Aii in Fig. 5 respectively. Similarly, Models Di and Dii shown in Fig. 5 are carotid models acquired for Artery D at baseline and follow-up respectively. The second column shows the 2D *VWT* maps and the third column shows the maps with "angular distortion" colour-coded and superimposed. The top sub-figures in the second and third columns show the maps generated by the previously described AL mapping algorithm, and the bottom sub-figures show the maps generated by the proposed conformal mapping algorithm. Each of the 2D AL and conformal maps was made up of 15,036 triangular elements. The angular distortion of each triangle element, denoted by $\Delta$ in Fig. 5, was quantified by the sum of the absolute average angular differences associated with its three angles: $\Delta = \frac{|\alpha-\tilde{\alpha}|+|\beta-\tilde{\beta}|+|\gamma-\tilde{\gamma}|}{3}$, where $\alpha$, $\beta$, $\gamma$ are the three angles of the triangle elements in the 3D map (first column), and $\tilde{\alpha}$, $\tilde{\beta}$, $\tilde{\gamma}$ are the corresponding angles in the 2D carotid template (third column). Figure 6 shows the average angular distortion for 10 arteries imaged at baseline, denoted by $T1$, and the follow-up session, denoted by $T2$. The reduction in the average angular distortion ranges from 1.7° to 5.1°. Two-sample $t$ test shows that the average angular distortion was significantly reduced after the conformal mapping operations described in Section 2.3.2 ($P = 2.06 \times 10^{-5}$).

Since all carotid arteries were mapped to a carotid template with the average surface areas over the entire cohort,

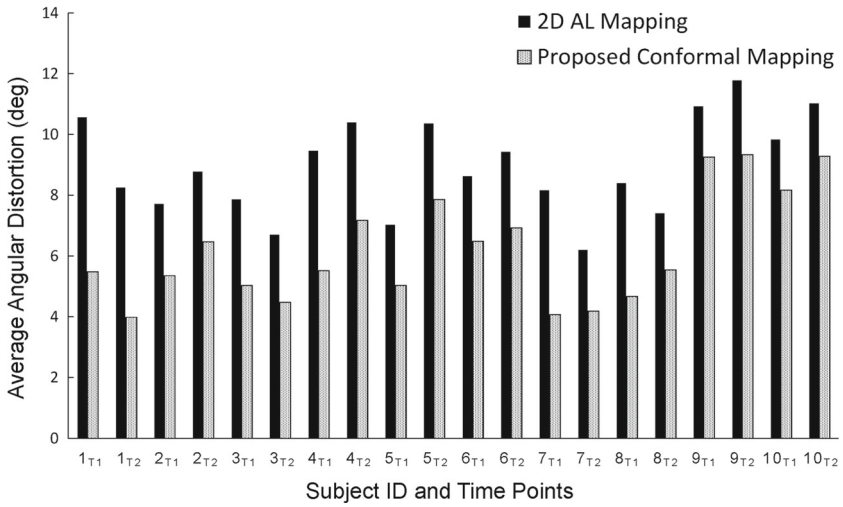


**Fig. 6** Average angular distortion of 20 carotid models. Each subject was scanned twice. The carotid models constructed from the baseline and follow-up 3D ultrasound images were denoted by the subscripts T1 and T2 respectively

areal distortion associated with the AL approach varies across arteries. The results displayed in Fig. 5 suggest that areal distortion is closely related to angular distortion. Arterial models Aii and B shown in Fig. 5 correspond to the models labelled $3_{T2}$ and $7_{T2}$ in Fig. 6. These two models had surface areas close to the group average, and the corresponding 2D AL maps had the smallest average angular distortion among carotid models involved in this study. Arterial models Ai and C correspond to the models labelled $3_{T2}$ and $6_{T1}$ in Fig. 6. As shown in Fig. 5Ai:3D and C:3D, these two models tapered off towards the CCA inlet, resulting in a larger areal distortion in the vicinity as shown in Fig. 5Ai:$\Delta_{AL}$ and C:$\Delta_{AL}$. Artery D corresponds to the Artery 10 labelled in Fig. 6. This artery had a surface area on the ICA side (i.e. the region represented by red in Fig. 4a) that was much smaller than the population average, leading to large angular distortions in the 2D AL map (Fig. 5Di:$\Delta_{AL}$, Dii:$\Delta_{AL}$). These angular distortions were minimized using the quasi-conformal mapping strategy as shown in the third column of Fig. 5. We also evaluated the angular distortion of 300,720 triangular elements in the 20 carotid models (15,036/carotid model $\times$ 20 models) before and after correction for angular distortion. Figure 7 shows the angular distortion histograms of the 2D AL maps and the maps generated by the proposed conformal mapping algorithm. The reduction in the angular distortion observed above was reflected by the fact that Fig. 7b skewed to the left as compared to Fig. 7a. However, it should be noted that the angular distortion was not perfectly 0 due to boundary constraints required for carotid template construction.

Although the application of the proposed algorithm led to a highly statistically significant decrease in angular distortion, the change in *VWT* distribution before and after angular correction was not visually apparent as shown in the second column of Fig. 5. This observation raises the question of whether the reduction of geometric distortion attained by the proposed algorithm has a clinical impact for *VWT* measurements. This study involves patients scanned 2 weeks apart with no physiological changes expected for them. The 2-week interscan interval was selected to maximize the variability from various sources, such as sonographer change, the difference in scanning parameters, image variability, registration error due to patient repositioning and the difference in neck orientations. Reduction of the variability on *VWT* due to better alignment produced by the proposed algorithm can be quantified by

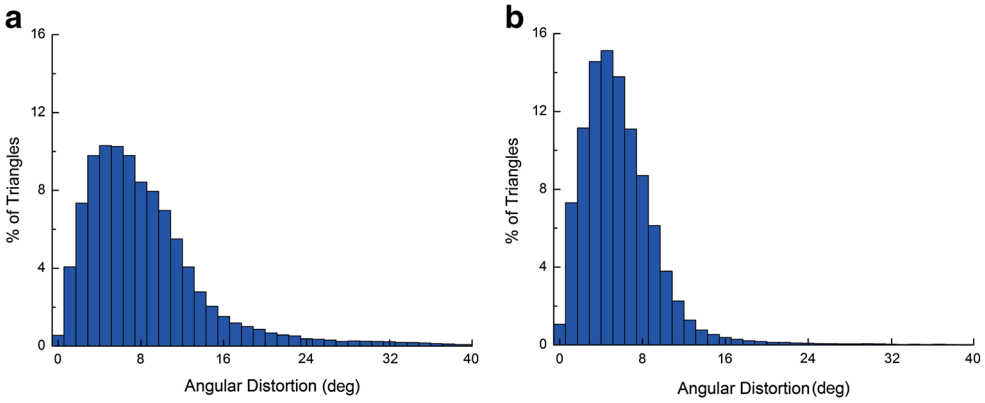


**Fig. 7** Histograms of angular distortions exhibited in 300,720 triangular elements (15,036/carotid model $\times$ 20 carotid models) in (**a**) the 2D AL maps and (**b**) the 2D conformal maps

the point-wise *VWT* difference ($\Delta VWT$) between the two scanning sessions. The reduction in the average absolute $\Delta VWT$ computed over the entire carotid map for each of the 10 patients after angular correction ranges from 1–5%. The amount of reduction for each artery was closely related to the amount of deformation required to correct the angular distortion, with Arteries A and D shown in Fig. 5 associated with the minimum and maximum reduction, respectively, among the studied cohort. In this pilot study for evaluating the proposed algorithm, the carotid surfaces obtained at baseline and follow-up were already fairly well aligned as exemplified by the 3D models of Arteries A and D displayed in Fig. 5, and for this reason, the impact on *VWT* measurements made by the proposed conformal mapping algorithm was not fully demonstrated in this cohort. Future clinical investigations involving subjects followed for a longer period will be required to assess the improvement on the reproducibility of *VWT* attained by the proposed algorithm.

Although the LBS and the Beltrami differential chopping methods were used as sub-steps in the algorithm designed to generate conformal spherical maps for the genus-0 brain surfaces [13], the performance of these methods to map to a non-convex domain, such as the L-shaped carotid template in the current application, has not been validated. Figure 8a shows the number of overlapping cells for the 20 arterial models before the application of the Beltrami differential smoothing and chopping approach, and Fig. 8b–e shows four 2D carotid maps associated with the largest number of overlapping cells. These figures show that all overlapping cells, represented in red, appeared in the neighborhood of the bifurcation. The application of the Beltrami differential smoothing and chopping approach described in Step 4 of Section 2.3.2 was able to generate bijective maps for all 20 arterial models (i.e. the number of overlapping cells were all 0 after the application of Step 4).

The 2D AL mapping algorithm was implemented in Visual Studio C++ and took 7 s to process each arterial model. The conformal mapping algorithm was implemented in Matlab and requires 2 s to process each model. Therefore, the total time for generating the conformal 2D *VWT* map was less than 10 s. All experiments were performed in an Intel(R) Core(TM) i7-3770 CPU @ 3.40 Hz with 8 GB memory.

## 4 Discussion

As carotid atherosclerosis is a focal disease predominantly occurring in bends and bifurcations, recent investigations pay particular attention to local biomarkers or risk factors,

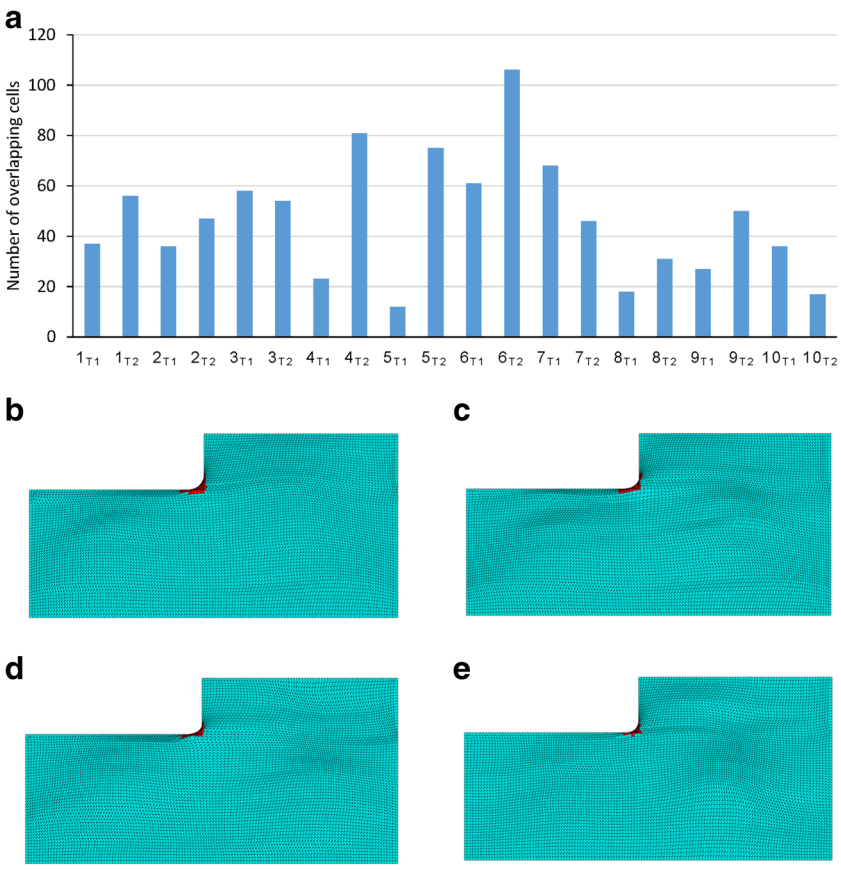


**Fig. 8** **a** Number of overlapping cells in 20 carotid models before the application of the Beltrami differential smoothing and chopping process (Step 4 of Section 2.3.2). Each map consisted of 15,036 triangular elements. **b–e** show the mapping for four example subjects with the highest number of overlapping cells in the study cohort. The overlapping cells are highlighted in *red* and predominantly occurred at the L-shaped corner representing the carotid bifurcation

including plaque and vessel wall thickness [6, 8–11], local hemodynamic forces [2, 3, 5, 19, 34], location of vulnerable plaque components [4, 19] and plaque fissures [7, 18]. As the geometry of arterial surfaces is highly subject-specific, there is a compelling need to map the patient-specific arterial model to a carotid template so that local properties can be objectively assessed in population studies aiming at identification and validation of local risk factors, as well as in the development of novel local biomarkers in evaluating the efficacy of treatment strategies. Although the AL approach previously described (Section 2.3.1) [10, 11] was developed for adjusting the geometric variability of a population of carotid arteries, this scheme did not consider the local geometric distortion produced by the 3D to 2D mapping. This paper introduced a framework to minimize the local angular distortion in the mapping process using quasi-conformal mapping theories.

Although many conformal mapping techniques have been developed previously, very few dealt with bifurcating vessels such as the carotid arteries. Notable exceptions include Antiga et al. [3] and Zhu et al. [39], and their limitations were thoroughly described in the introduction to motivate the development of the proposed method. In summary, four major properties should be taken into consideration when designing a mapping technique used in carotid template construction and, in fact, were considered when the AL approach was developed: (1) The boundary of the carotid template must be fixed. (2) The boundary of the carotid template represents geometrically correspondence points of arteries. (3) The resulting 2D planar map should be continuous from the CCA to ICA to facilitate quantification and visualization of carotid plaques located at the bifurcation and near the carotid bulb. (4) The distance of a surface point from the carotid bifurcation should be represented in a consistent way for all subjects in the 2D planar map. The algorithm introduced by Zhu et al. [39] lacks Properties (1) and (2), and that by Antiga et al. [3] lacks Property (3).

As the AL maps have many properties suitable for carotid template construction, in developing the first conformal mapping strategy that has the above four properties desirable for carotid template construction, the proposed framework focused on minimizing local geometric distortion generated by the AL mapping strategy. The central idea of the proposed optimization approach is to compute a map to compensate for the angular distortion produced in the AL mapping procedure based on results established in the quasi-conformal mapping theory. Mathematically, computing such a map involved finding out its Beltrami differential, $\mu$, from which the map can be constructed by a previously described technique known as the Linear Beltrami Solver (LBS) [30]. A desirable property of the proposed optimization framework is that the LBS algorithm can incorporate boundary correspondence points established by the AL approach when computing the map required for correcting angular distortion. Since the algorithm only involves solving a few sparse linear systems, the computation is highly efficient. Unlike in previous publications [14, 32, 36] where surfaces were mapped to a fixed-boundary convex planar domain (e.g., circular disk and rectangle), the carotid template described in this paper lies on an L-shaped non-convex domain. For this reason, there is no guarantee that the map generated by the LBS algorithm is bijective. Since a map is bijective if and only if the norm of $\mu$ is smaller than unity, the norm of $\mu$ was chopped and $\mu$ was smoothed in an iterative manner to enforce bijectivity. Although this chopping algorithm has been applied previously to map cortical surfaces to a sphere [13], for the first time, the current study has validated the chopping approach for mapping onto a non-convex planar domain.

There are a number of limitations in this study on the technical side as well as the application aspects. Future investigations will be performed to address these issues. The first limitation is that the proposed algorithm cannot completely eliminate the angular distortion produced by AL mapping due to the boundary constraints. Although the distortion inside the L-shaped domain has largely been corrected by the proposed technique, the angular distortion near the boundary was not negligible. A possible improvement of this technique we will implement involves relaxing the boundary constraints by allowing points to move along the boundary. Although the improved technique will still be susceptible to boundary constraints and angular distortion would still exist, we expect the angular distortion along the boundary to be further reduced. A full investigation will be performed to validate this hypothesis rigorously. Another limitation is related to the use of a small group of subjects in this evaluation study for a novel algorithm. In this study, the expert observer took 20–30 min to segment the lumen and outer wall from a 3D ultrasound image. As five repeated segmentations for each image were performed to reduce the effect of segmentation variability, segmentation for 20 images already took a considerable amount of time. While we acknowledge that the geometric variability of carotid vessels may not be sufficiently represented by the cohort involved in this study, it is sensible to perform a pilot study to validate the performance of our novel approach before carrying out an evaluation study involving a larger population. With the performance of the algorithm demonstrated in this study, we are currently incorporating the new mapping approach into our established pipeline [8–10] in analyzing patient data available from ongoing clinical studies aiming at evaluating statin and vitamin B treatments.

In addition to providing a more consistent display for the distribution of local quantities on carotid surfaces to facilitate visual comparison, the proposed algorithm is expected to improve the sensitivity of *VWT*-based biomarkers

developed based on the carotid template. A major extension of the current work will involve quantitative evaluation of the sensitivity improvement in detecting treatment effects by such biomarkers. One such example is the region-based biomarkers developed in one of our clinical studies focusing on evaluating the effect of atorvastatin in the progression/regression of carotid atherosclerosis [10]. Briefly, the biomarker quantified the average *VWT-Change* specific to regions of interest identified on the 2D *VWT* maps by a feature selection algorithm. This biomarker contributed to a three-fold reduction in the sample size required to establish a statistically significant difference between the atorvastatin and placebo groups, as compared to the average *VWT-Change* over the entire carotid template and vessel wall volume measurements. Since the proposed algorithm has improved the consistency of the 2D *VWT* map representation by reducing local geometry distortion, we hypothesize that the sensitivity of the region-specific average $\Delta VWT$ biomarker to be further improved. A full study will be required to validate this hypothesis and investigate the extent of the improvement. Further reduction of sample size required to detect treatment effects will allow many pilot clinical studies to be performed to establish efficacy of novel treatment strategies before a more costly study involving a larger population and spanning a longer time frame is held to validate the result.

## 5 Conclusion

The motivation of this work stems from the need to compare the spatial distributions of *VWT* in a population of subjects consistently and quantitatively in longitudinal and cross-sectional studies for stroke risk assessment and evaluation of treatment options. In this paper, we developed and validated a fast and automatic conformal mapping technique to adjust for the anatomic variability of carotid surface models within 10 s. Our results show that the reduction in the local angular distortion made by the proposed algorithm was statistically highly significant. In addition, our study validated for the first time that the iterative Beltrami differential smoothing and chopping approach was able to enforce bijective mapping onto a non-convex domain, the L-shaped carotid template in this study. In addition to providing a more consistent display of the spatial *VWT* distribution for each patient to enhance visual comparison, the reduction in local geometry distortion attained in this study will reduce the bias in VWT-based biomarkers previously introduced [6, 10] and potentially improve the sensitivity of such biomarkers.

**Acknowledgements** Dr. Chiu is grateful for funding support from the Research Grant Council of the HKSAR, China (Project No. CityU 139713), the National Natural Science Foundation of China (Grant No. 81201149), the Basic Research Free Exploration Program of the Science Technology and Innovation Committee of Shenzhen Municipality, China (Project No. JCYJ20160428155118212) and the City University of Hong Kong Strategic Research Grants (Nos. 7004425 and 7004617). The authors also acknowledge Dr. Aaron Fenster for providing the 3D ultrasound images and manually segmented contours for this work.

## References

1. Ainsworth CD, Blake CC, Tamayo A, Beletsky V, Fenster A, Spence JD (2005) 3D ultrasound measurement of change in carotid plaque volume: a tool for rapid evaluation of new therapies. Stroke 36(9):1904–1909. doi:10.1161/01.STR.0000178543.19433.20
2. Antiga L, Piccinelli M, Botti L, Ene-Iordache B, Remuzzi A, Steinman DA (2008) An image-based modeling framework for patient-specific computational hemodynamics. Med Biol Eng Comput 46:1097–1112. doi:10.1007/s11517-008-0420-1
3. Antiga L, Steinman DA (2004) Robust and objective decomposition and mapping of bifurcating vessels. IEEE Trans Med Imaging 23(6):704–713. doi:10.1109/TMI.2004.826946
4. Canton G, Chiu B, Chen H, Chen Y, Hatsukami TS, Kerwin WS, Yuan C (2013) A framework for the co-registration of hemodynamic forces and atherosclerotic plaque components. Physiol Measur 34:977–990. doi:10.1088/0967-3334/34/9/977
5. Chen Y, Canton G, Kerwin WS, Chiu B (2016) Modeling hemodynamic forces in carotid artery based on local geometric features. Med Biol Eng Comput 54:1437–1452. doi:10.1007/s11517-015-1417-1
6. Cheng J, Pike D, Chow TW, Kirby M, Parraga G, Chiu B (2016) Three-dimensional ultrasound measurements of carotid vessel wall and plaque thickness and their relationship with pulmonary abnormalities in ex-smokers without airflow limitation. Int J Cardiovasc Imaging 32(9):1391–1402
7. Chiu B, Beletsky V, Spence JD, Parraga G, Fenster A (2009) Analysis of carotid lumen surface morphology using three-dimensional ultrasound imaging. Phys Med Biol 54(5):1149–1167. doi:10.1088/0031-9155/54/5/004
8. Chiu B, Chen W, Cheng J (2016) Concise biomarker for spatial-temporal change in three-dimensional ultrasound measurement of carotid vessel wall and plaque thickness based on a graph-based random walk framework: towards sensitive evaluation of response to therapy. Comput Biol Med 79:149–162
9. Chiu B, Egger M, Spence JD, Parraga G, Fenster A (2008) Quantification of carotid vessel wall and plaque thickness change using 3D ultrasound images. Med Phys 35(8):3691–3710. doi:10.1118/1.2955550
10. Chiu B, Li B, Chow TWS (2013) Novel 3d ultrasound image-based biomarkers based on a feature selection from a 2d standardized vessel wall thickness map: a tool for sensitive assessment of therapies for carotid atherosclerosis. Phys Med Biol 58(17):5959–5982. doi:10.1088/0031-9155/58/17/5959
11. Chiu B, Ukwatta E, Shavakh S, Fenster A (2013) Quantification and visualization of carotid segmentation accuracy and precision using a 2D standardized carotid map. Phys Med Biol 58(11):3671–3703. doi:10.1088/0031-9155/58/11/3671
12. Choi GPT, Lui LM (2017) A linear formulation for disk conformal parameterization of simply-connected open surfaces. Adv Comput Math 1–28. doi:10.1007/s10444-017-9536-x
13. Choi PT, Lam KC, Lui LM (2015) FLASH: fast landmark aligned spherical harmonic parameterization for genus-0 closed brain surfaces. SIAM J Imaging Sci 8(1):67–94. doi:10.1137/130950008

14. Choi PT, Lui LM (2015) Fast disk conformal parameterization of simply-connected open surfaces. J Sci Comput 65(3):1065–1090
15. Egger M, Chiu B, Spence JD, Fenster A, Parraga G (2008) Mapping spatial and temporal changes in carotid atherosclerosis from three-dimensional ultrasound images. Ultrasound Med Biol 34(1):64–72. doi:10.1016/j.ultrasmedbio.2007.07.004
16. Eicke BM, von Lorentz J, Paulus W (1995) Embolus detection in different degrees of carotid disease. Neurol Res 17(3):181–184
17. Fenster A, Downey DB (2000) Three-dimensional ultrasound imaging. Annu Rev Biomed Eng 2:457–475
18. Fenster A, Landry A, Downey DB, Hegele RA, Spence JD (2004) 3D ultrasound imaging of the carotid arteries. Curr Drug Targets Cardiovasc Haematol Disord 4(2):161–175
19. Filipovic N, Teng Z, Radovic M, Saveljic I, Fotiadis D, Parodi O (2013) Computer simulation of three-dimensional plaque formation and progression in the carotid artery. Med Biol Eng Comput 51(6):607–616. doi:10.1007/s11517-012-1031-4
20. Floater MS, Hormann K (2005) Surface parameterization: a tutorial and survey, pp. 157–186. Advances in multiresolution for geometric modelling. Springer-Verlag, Heidelberg
21. Haker S, Angenent S, Tannenbaum A, Kikinis R (2000) Nondistorting flattening maps and the 3-D visualization of colon CT images. IEEE Trans Med Imaging 19(7):665–670
22. He J, Gu D, Wu X, Reynolds K, Duan X, Yao C, Wang J, Chen CS, Chen J, Wildman RP, Klag MJ, Whelton PK (2005) Major causes of death among men and women in china. N Engl J Med 353(11):1124–1134. doi:10.1056/NEJMsa050467
23. Krasinski A, Chiu B, Fenster A, Parraga G (2009) Magnetic resonance imaging and three-dimensional ultrasound of carotid atherosclerosis: mapping regional differences. J Magn Reson Imaging 29(4):901–908. doi:10.1002/jmri.21709
24. Krasinski A, Chiu B, Spence JD, Fenster A, Parraga G (2009) Three-dimensional ultrasound quantification of intensive statin treatment of carotid atherosclerosis. Ultrasound Med Biol 35(11):1763–1772. doi:10.1016/j.ultrasmedbio.2009.05.017
25. Kwon TG, Kim KW, Park HW, Jeong JH, Kim KY, Bae JH (2009) Prevalence and significance of carotid plaques in patients with coronary atherosclerosis. Korean Circ J 39:317–321. doi:10.4070/kcj.2009.39.8.317
26. Landry A, Spence JD, Fenster A (2004) Measurement of carotid plaque volume by 3-dimensional ultrasound. Stroke 35(4):864–869
27. Lee SW, Antiga L, Spence JD, Steinman DA (2008) Geometry of the carotid bifurcation predicts its exposure to disturbed flow. Stroke 39:2341–2347. doi:10.1161/STROKEAHA.107.510644
28. Liu L, Wang D, Wong KSL, Wang Y (2011) Stroke and stroke care in china: huge burden, significant workload, and a national priority. Stroke 42:3651–3654. doi:10.1161/STROKEAHA.111.635755
29. Liu M, Wu B, Wang WZ, Lee LM, Zhang SH, Kong LZ (2007) Stroke in china: epidemiology, prevention, and management strategies. Lancet Neurol 6(5):456–464. doi:10.1016/S1474-4422(07)70004-2
30. Lui LM, Lam KC, Wong TW, Gu X (2013) Texture map and video compression using Beltrami representation. SIAM J Imag Sci 6(4):1880–1902. doi:10.1137/120866129
31. Malek AM, Alper SL, Izumo S (1999) Hemodynamic shear stress and its role in atherosclerosis. JAMA 282(21):2035–2042
32. Meng TW, Choi GPT, Lui LM (2016) TEMPO: feature-endowed Teichmüller extremal mappings of point clouds. SIAM J Imaging Sci 9(4):1922–1962
33. Mozaffarian D, Benjamin EJ, Go AS, Arnett DK, Blaha MJ, Cushman M, de Ferranti S, Després JP, Fullerton HJ, Howard VJ, Huffman MD, Judd SE, Kissela BM, Lackland DT, Lichtman JH, Lisabeth LD, Liu S, Mackey RH, Matchar DB, McGuire DK, Mohler ER, Moy CS, Muntner P, Mussolino ME, Nasir K, Neumar RW, Nichol G, Palaniappan L, Pandey DK, Reeves MJ, Rodriguez CJ, Sorlie PD, Stein J, Towfighi A, Turan TN, Virani SS, Willey JZ, Woo D, Yeh RW, Turner MB (2014) Heart disease and stroke statistics - 2015 update. Circulation. doi:10.1161/CIR.0000000000000152
34. Perktold K, Thurner E, Kenner T (1994) Flow and stress characteristics in rigid walled and compliant carotid artery bifurcation models. Medi Biol Eng Comput 32:19–26
35. Spence JD (2007) Intensive management of risk factors for accelerated atherosclerosis: the role of multiple interventions. Curr Neurol Neurosci Rep 7(1):42–48. doi:10.1007/s11910-007-0020-8
36. Yang YL, Guo R, Luo F, Hu SM, Gu X (2009) Generalized discrete ricci flow. Comput Graph Forum 28(7):2005–2014. doi:10.1111/j.1467-8659.2009.01579.x
37. Zeng W, Lui LM, Luo F, Chan TFC, Yau ST, Gu DX (2012) Computing quasiconformal maps using an auxiliary metric and discrete curvature flow. Numerische Mathematik 121(4):671–703. doi:10.1007/s00211-012-0446-z
38. Zeng W, Marino J, Gurijala KC, Gu X, Kaufman A (2010) Supine and prone colon registration using quasi-conformal mapping. IEEE Trans Vis Comput Graph 16(6):1348–1357
39. Zhu L, Haker S, Tannenbaum A (2005) Flattening maps for the visualization of multibranched vessels. IEEE Trans Med Imaging 24(2):191–198. doi:10.1109/TMI.2004.839368

**Gary P. T. Choi** received his BSc and MPhil degrees in Mathematics from The Chinese University of Hong Kong in 2014 and 2016 respectively. He is currently an Applied Mathematics Ph.D. student in the John A. Paulson School of Engineering and Applied Sciences at Harvard University. His research interests include computational differential geometry, medical imaging, mathematical modeling and scientific computing.

**Yimin Chen** is currently a computer vision researcher in SenseTime, Shenzhen, China. He received his bachelor and master degrees in Biomedical Engineering from Huazhong University of Science and Technology in 2009 and 2012, respectively, and his Ph.D. degree in Electronic Engineering from City University of Hong Kong in 2016. His research includes medical image processing and analysis.

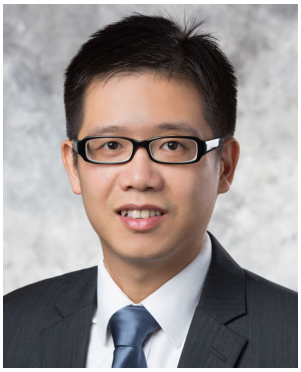

**Lok Ming Lui** an Associate Professor in the Mathematics department of The Chinese University of Hong Kong (CUHK). He got his PhD in Applied Mathematics at UCLA Math department in June, 2008, under the supervision of Prof. Tony F. Chan. Before joining CUHK, he worked as a Postdoctoral Scholar for 2 years at Harvard Math department, hosted by Prof. Shing-Tung Yau. He was awarded the Morningside Mathematics (Silver) Medal during the International Congress of Chinese Mathematicians in 2016. His research interest includes Computational conformal/quasi-conformal geometry; medical imaging; and mathematical shape analysis.

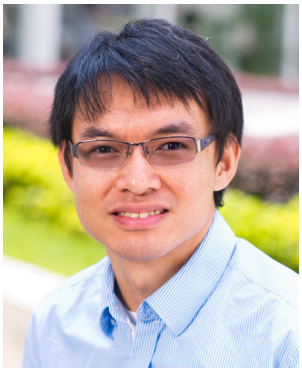

**Bernard Chiu** is currently an Assistant Professor in the Department of Electronic Engineering at the City University of Hong Kong. He received his Bachelor of Science degree in Electrical Engineering at the University of Calgary, Canada, in 2001, his Master of Applied Science degree in Electrical and Computer Engineering at the University of Waterloo, Canada, in 2003, and his PhD in Biomedical Engineering at the University of Western Ontario, Canada, in 2008. He was a Senior Fellow in the Department of Radiology at the University of Washington, Seattle, USA before joining City University of Hong Kong. His research focuses on the development of novel image processing, quantification and visualization methods in the fields of cardiovascular risk assessment and monitoring as well as in oncology.